Dalton Transactions

ROYAL SOCIETY OF CHEMISTRY

PAPER

View Article Online
View Journal | View Issue

Cite this: *Dalton Trans.*, 2025, **54**, 8214

Monitoring CO as a plant signaling molecule under heavy metal stress using carbon nanodots†

Shrodha Mondal,[a] Olivia Sarkar,[b] Santi M. Mandal,[c] Ansuman Chattopadhyay[b] and Prithidipa Sahoo *[a]

Carbon monoxide (CO) is widely recognized as a significant environmental pollutant and is associated with numerous instances of accidental poisoning in humans. However, it also serves a pivotal role as a signaling molecule in plants, exhibiting functions analogous to those of other gaseous signaling molecules, including nitric oxide (NO) and hydrogen sulfide (H_2S). In plant physiology, CO is synthesized as an integral component of the defense mechanism against oxidative damage, particularly under abiotic stress conditions such as drought, salinity, and exposure to heavy metals. Current research methodologies have demonstrated a lack of effective tools for monitoring CO dynamics in plants during stress conditions, particularly in relation to heavy metal accumulation across various developmental stages. Therefore, development of a sensor capable of detecting CO in living plant tissues is essential, as it would enable a deeper understanding of its biological functions, underlying mechanisms, and metabolic pathways. In response to this gap, the present study introduces a novel technique for monitoring CO production and activity in plants using nitrogen-doped carbon quantum dots (N-CQDs). These nanodots exhibited exceptional biocompatibility, low toxicity, and environmentally sustainable characteristics, rendering them an optimal tool for CO detection *via* fluorescence quenching mechanism, with a detection limit (LOD) of 0.102 μM. This innovative nanomarker facilitated the detection of trace quantities of CO within plant cells, providing new insights into plant stress responses to heavy metals such as Cu, Zn, Pb, Ru, Cr, Cd, and Hg, as well as the processes involved in seed germination. Additionally, confocal microscopy validated the interaction between CO and N-CQDs, yielding visual evidence of CO binding within plant cells, further enhancing the understanding of CO's role in plant biology.

Received 5th November 2024,
Accepted 28th December 2024

DOI: 10.1039/d4dt03101f

rsc.li/dalton

Introduction

For centuries, carbon monoxide has been considered as a harmful gas to humans; however, recent studies have revealed its important signaling role in plants.[1,2] By generating a wide range of defense-related hormones that trigger intricate regulatory networks, plants in biological environments establish inducible defensive systems to endure biotic and abiotic stresses. Carbon monoxide (CO) is also produced as a defense mechanism against oxidative damage under abiotic stressors, such as drought, salinity, and exposure to heavy metals.[3–5] Similar to other gasotransmitters, such as NO and H_2S, CO needs to be present to participate in plant physiological activities. Previous research has identified three crucial pathways for CO production in living organisms.[6,7] The first pathway involves lipid peroxidation and ureide metabolism. Lipid peroxidation requires nicotinamide adenine dinucleotide phosphate (NADPH) for CO production and occurs in various plants as well as mammalian tissues and cells. During ureide metabolism, glyoxylate from urea catabolism may be formed, potentially leading to the production of CO. The second pathway involves the photo-oxidation of organic compounds within plants, likely due to direct photochemical transformations within the plant matrix. The third pathway involves degradation catalyzed by heme oxygenase (HO), an enzyme responsible for CO production, free iron, and biliverdin (BV). This pathway specifically occurs in plants, and HOs are still considered the primary enzymatic source of endogenous CO in plants.[8–10] These three pathways demonstrate the diverse mechanisms through which CO is generated in living organisms. CO influences development of seedlings, including stress responses, root growth, and germination.[11–15] It promotes seedling growth and increases resistance to environmental stressors by interacting with plant hormones such as

[a]*Department of Chemistry, Visva-Bharati University, Santiniketan-731235, India. E-mail: prithidipa.sahoo@visva-bharati.ac.in*
[b]*Department of Zoology, Visva-Bharati University, Santiniketan-731235, India*
[c]*Department of Biotechnology, Indian Institute of Technology Kharagpur, Kharagpur-721302, India*

† Electronic supplementary information (ESI) available. See DOI: https://doi.org/10.1039/d4dt03101f

auxins and gibberellins. The signaling function of CO is related to antioxidant activity and regulates the reactive oxygen species (ROS) levels in seedlings under oxidative stress. Additionally, CO has been shown to reduce the absorption of Cd in plants and alleviate Cd stress by regulating transcription factors and transporter genes. CO is found to alleviate stress due to other heavy metals such as Cu, Zn, Pb, Ru, Cr, and Hg by regulating the antioxidant system. These results indicate that under controlled conditions, CO may have a protective and regulatory role in early plant development and stress adaptation.[8]

As a result, an increasing interest among researchers for investigating the functions and presence of CO in plant systems has been noted. There remains a lack of comprehensive methodologies for effectively monitoring CO within plant cells and tissues. Compared to previous techniques, our proposed method offers a biocompatible, simple, and cost-effective approach to synthesize a nontoxic nanosensor capable of detecting CO at low concentrations. This advancement enables real-time monitoring of CO dynamics within plant systems, as demonstrated under heavy metal stress conditions. Unlike some previous works that have utilized Pd, chemosensors, or dyes that are not biocompatible, water-soluble, cost-effective and are often toxic, our method prioritizes environmental and biological compatibility. The published processes are quite complicated and time consuming. The performance metrics, provided in Table S1,† underscore the sensor's sensitivity and practicality, positioning it as a valuable tool for studying plant signaling pathways. Carbon quantum dots (CDs) have attracted considerable scholarly attention in recent years for their versatile applications in sensing and imaging due to their distinctive optical characteristics and surface functionalities. Recent studies have explored the synthesis and functionalization of CDs for specific applications, such as environmental monitoring,[16] energy production,[17] catalysis,[18] chemical sensing,[19] as well as biosensing platforms.[20] Building on these advances, the present study developed a novel nanomarker utilizing nitrogen-doped carbon quantum dots (N-CQDs) (3-aminophenol and diethylenetriamine) with unique fluorescence quenching properties, thus enabling the detection and monitoring of carbon monoxide (CO) as a signaling molecule in plants under heavy metal stress. These N-CQDs demonstrate high biocompatibility, low toxicity, and an environment-friendly profile, thereby facilitating the detection of trace amounts of CO within plant cells. This successful synthesis of fluorescent nanodots for CO monitoring represents a significant advancement in understanding CO's role in alleviating heavy metal stress in plant systems. This study facilitates the real-time tracking of CO and its pathways within plant organisms, thereby offering novel insights into the dynamic responses of plants subjected to environmental stressors. Integrating CO-sensing technology with the biological study of plants not only enhances comprehension of the mechanisms underlying plant resilience but creates opportunities for future research directed toward agricultural stress management and environmental monitoring.

In our prior research, this quantum dot-based sensor was developed for CO detection, with specific applications aimed at ensuring human safety, primarily due to the harmful effects of CO as a toxic gas. The present study illustrates the transition from emphasizing CO as a hazardous agent to exploring its vital role as a signaling molecule within plant systems. Recent investigations have indicated that, under controlled concentrations, CO acts as a crucial mediator in various physiological processes of plants, including their responses to environmental stressors, such as heavy metal toxicity. This affirms the multifunctionality of the nanosensors and explains their applicability in technological, agricultural, and biological contexts.

Experimental

Materials and methods

All analytes, including nitric oxide, carbon monoxide, nicotine, hydrogen peroxide, 3-aminophenol, and diethylenetriamine, were obtained from TCI India and Sigma-Aldrich and utilized exactly as supplied, requiring no additional purification. Double-distilled water was used as the solvent.

Preparation and characterization of N-CQDs

Nitrogen-doped carbon quantum dots (N-CQDs) have been produced utilizing a domestic microwave oven. The precursor materials selected for this synthesis, *i.e.*, 3-aminophenol and diethylenetriamine, were chosen due to their significant nitrogen and carbon content, as illustrated in Scheme 1. Detailed descriptions of the synthesis conditions and procedural steps are provided in the ESI.† A complete characterization of N-CQDs was conducted employing a diverse range of spectroscopic and microscopic techniques. Dynamic light scattering (DLS) and transmission electron microscopy (TEM) were utilized to assess the size distribution and morphology of the dots. Fourier transform infrared (FT-IR) spectroscopy and energy dispersive X-ray spectroscopy (EDX) were applied to study the surface functional groups and chemical structure. The optical properties, including UV absorption and fluorescence characteristics, were analyzed using a UV-visible spectrophotometer and a fluorimeter, respectively. Furthermore, fluorescence lifetimes were quantified through time-correlated single-photon counting (TCSPC), and the elemental composition was determined *via* X-ray photoelectron spectroscopy (XPS). Confocal laser scanning microscopy (CLSM) was used to generate confocal images. Further details and findings are available in the ESI.†

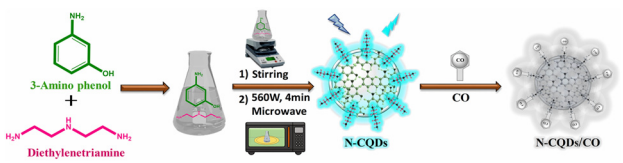

Scheme 1 A diagrammatic representation of the process for synthesizing N-CQDs in a home microwave using 3-amino phenol and diethylenetriamine.

CO detection process

In the preparation of the N-CQDs solution, 200 μL of the synthesized N-CQDs was diluted with 1.8 mL of DD water within a quartz cuvette. Subsequently, this diluted solution was then treated with varying concentrations of CO derived from a 10^{-4} M stock solution. Fluorescence spectra were subsequently acquired by exciting the solution at a wavelength of 320 nm.

Determination of quantum yield (QY)

The quantum yield (QY) of N-CQDs was calculated using the following equation[21] employing quinine sulfate as the reference standard, which possesses a known quantum yield of 0.54.

$$Q_x = Q_{st}(I_x/I_{st})(A_{st}/A_x)(n_x^2/n_{st}^2) \quad (1)$$

In this expression, the variable "x" is indicative of the sample, while "st" denotes the standard (quinine sulfate) with a predetermined quantum yield. The variables 'I' represent the observed integrated emission intensity, 'A' signifies the absorbance at 320 nm, 'n' refers to the refractive index, and 'Q' indicates the quantum yield of the N-CQDs. To minimize the effects of reabsorption, the absorbance of each solution was upheld below 0.05 at the excitation wavelength of 320 nm. Additional details, along with a graphical representation of the measurements, are provided in Fig. S1.†

Experimental design and confocal laser scanning microscopy (CLSM) analyses

The uptake of CO and heavy metals (analytes) and evaluation of the efficiency and permeability of quantum dots (N-CQDs) (probes) into biological systems were substantiated utilizing embryonic roots and seeds of two plant species, namely, black chickpea (*Cicer arietinum*) and mung bean (*Vigna radiata*). The experiment involved four distinct groups of plants for each species.

The first group, selected as the control, remained untreated without any exposure to either the analyte or probe. The second group of plants was treated with heavy metals (10^{-3} M) for 12 hours. The third group was treated with a low concentration of the synthesized N-CQDs (10^{-3} M) for 12 hours following a prior 12-hour exposure to heavy metals at a concentration of 10^{-3} M. The fourth set was treated with a low dose of CO (10^{-3} M) for 12 hours after treatment with heavy metals (10^{-3} M) and N-CQDs (10^{-3} M) for 12 hours each.

Once all the treatment phases were finished, thin transverse sections were cut from both the embryonic roots and seeds of untreated and treated black chickpeas and mung beans. These slices were placed in watch glasses containing an equal mixture of double-distilled water and glycerol. The sections were then gently moved onto glass slides and covered with cover slips, allowing for examination using a confocal microscope.

A Leica TCS SP8 laser scanning confocal microscope system was used to capture confocal microscopic images. LasX software facilitated analysis of the images obtained through section scanning. A blue channel filter was employed with an excitation wavelength of 320 nm and an emission wavelength of 390 nm. The images were captured at a magnification of 10×.

Results and discussion

Morphological analysis

The TEM images presented in Fig. 1A highlight the spherical morphology of N-CQDs, with particles exhibiting a uniform dispersion and the absence of visible agglomeration. The distribution of particle sizes for N-CQDs is found to range from 1.1 to 3.3 nm, with an average diameter of around 2.1 nm, which aligns with the DLS data depicted in Fig. 1B. Furthermore, the high-resolution TEM (HRTEM) image presented as an inset in Fig. 1A reveals distinct lattice fringes in numerous particles, confirming their crystalline structure with a lattice spacing measured at 0.1867 nm. This crystalline characteristic was further validated by the circular ring pattern observed in the selected area electron diffraction (SAED) image shown in Fig. 1C.[22]

Fig. 1D presents the results of FTIR spectroscopy, which was performed to elucidate the surface functional groups present in N-CQDs. The analysis reveals broad absorption bands observed in the 3100–3500 cm^{-1} region, which are indicative of O–H and N–H vibrational modes. Furthermore, the absorption band located at 2914 cm^{-1} can be attributed to C–H stretching vibrations. The spectral signals detected between 1640 and 1550 cm^{-1} are associated with N–H bending vibrations, thereby confirming the presence of amino functional groups on the surface of N-CQDs. Notably, a characteristic peak observed at 1398 cm^{-1} serves as evidence for nitrogen doping, specifically associated with C–N bond formation. Additionally, the absorption features identified in the range of 1000–1300 cm^{-1} suggest the presence of C–O, C–N, and N–H bonds, further supporting the characterization of the functional groups on the N-CQD surface.[23–27] The interaction between CO and the surface groups of N-CQDs was further clarified with the generation of CO stretching frequency at 1965 cm^{-1} (Fig. S2†). The shifts in absorption peaks indicate the formation of a ground-state complex between CO and these functional groups, which likely contributes to the fluorescence quenching mechanism. Also, the variations in peak intensity suggest alterations in the vibrational modes, potentially due to CO adsorption or bonding.

The structural characteristics and elemental composition of N-CQDs were examined through XPS and EDX analyses. The EDX spectrum, as illustrated in Fig. 1E, affirmed the presence of carbon (C), oxygen (O), and nitrogen (N), corroborating the findings obtained from the XPS results shown in Fig. 1F. The XPS survey spectrum displayed prominent peaks corresponding to binding energies of C 1s, N 1s, and O 1s at 283.1 eV, 399.3 eV, and 530.2 eV, respectively (Fig. 1F). Furthermore, the high-resolution XPS spectra for C 1s, as depicted in Fig. S3A,† revealed two significant peaks at 284.5 eV and 285.5 eV, indicative of C–C/C–H and C–N/C–O bonds, respectively. The presence of nitrogen doping was further substantiated by

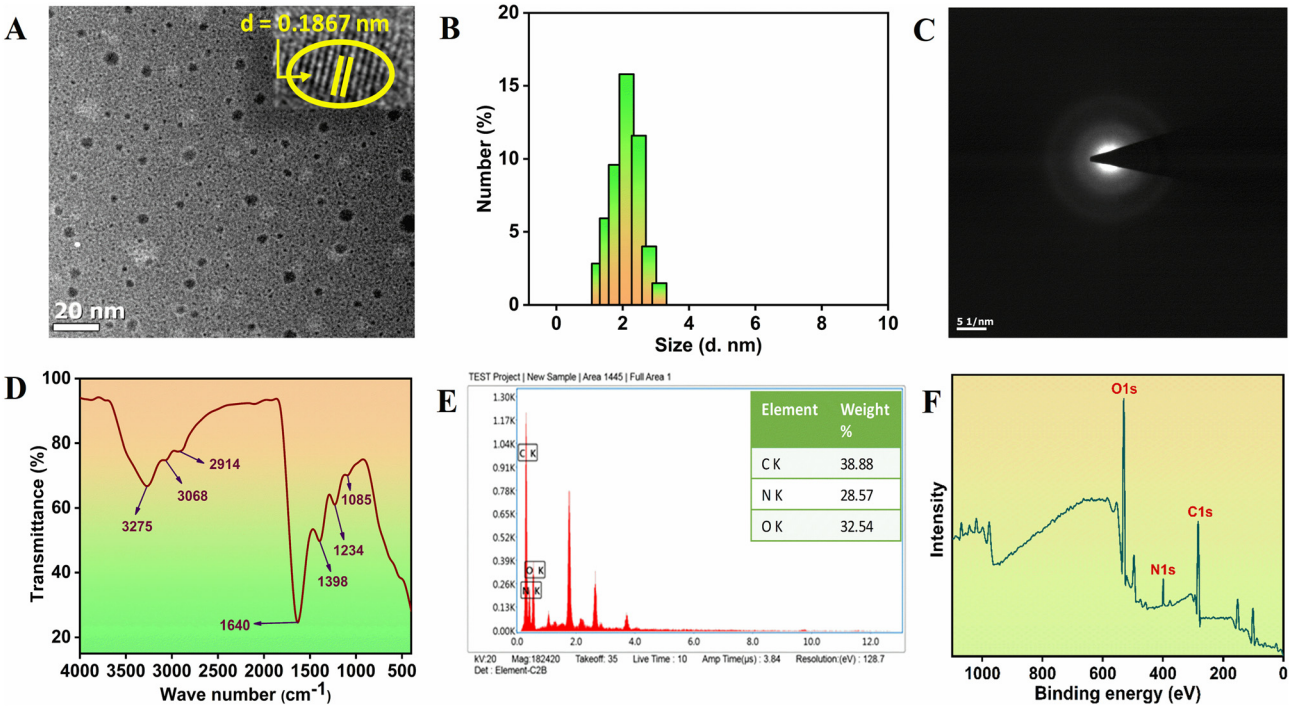

Fig. 1 (A) TEM (inset: HRTEM) image, (B) DLS analysis, (C) SAED analysis, (D) FT-IR spectra, (E) EDX data and (F) XPS survey spectra of N-CQDs.

the N 1s spectra presented in Fig. S3B,† which exhibited peaks attributable to pyridinic nitrogen (C–N–C, C═N), pyrrolic nitrogen (C_3–N), and N–H, located at binding energies of 399.5 eV, 400.1 eV, and 401.2 eV, respectively. In addition, the O 1s spectra, demonstrated in Fig. S3C,† exhibited peaks at 531.5 eV and 532.5 eV, corresponding to C═O and C–O–H functional groups, respectively.[28–31]

Optical properties of N-CQDs

The ultraviolet-visible (UV-Vis) absorption spectrum of N-CQDs, as illustrated in Fig. 2A, reveals two distinct peaks: the first at 298 nm within the 250–300 nm range, and a shoulder peak at 455 nm. The peak at 298 nm is indicative of the characteristic absorption properties associated with aromatic pi systems, which are analogous to those observed in polycyclic aromatic hydrocarbons. Conversely, the absorption feature observed at 455 nm suggests the indicative of nitrogen doping within the carbon quantum dots.[32,33] N-CQDs exhibited their most pronounced fluorescence emission at 389 nm when excited at a wavelength of 320 nm, a phenomenon presented in Fig. 2B. Furthermore, they demonstrated significant solubility and emitted a vibrant blue fluorescence upon exposure to ultraviolet (UV) light, as shown in the inset of Fig. 2B. The maximum fluorescence intensity was recorded at an excitation wavelength of 320 nm, accompanied by a gradual redshift and a corresponding decline in intensity (Fig. 2C). The fluorescence quantum yield (FLQY) of the N-CQDs was computed to be approximately 39%, as indicated in Fig. S1.† A study examining pH stability was conducted both in the presence and absence of CO, revealing that the fluorescence intensity remained stable within the pH range of 7–9 in both experimental conditions (Fig. 2D). The photostability of N-CQDs was extensively evaluated through exposure to continuous UV irradiation at 365 nm; the results demonstrated that even after 240 minutes of sustained exposure, the fluorescence intensity exhibited negligible change, as illustrated in Fig. 2E. This highlights the remarkable photostability and resistance of N-CQDs against photodegradation under extended UV irradiation. Besides, the fluorescence intensity was stable even after several months of storage when subsequently re-exposed to UV light at 365 nm.

Fluorescence detection of N-CQDs in the presence of CO

To assess the efficacy of N-CQDs as a sensor for CO, a solution with a concentration of 10^{-4} M CO was added into the N-CQDs solution, followed by an analysis of the resultant fluorescence spectra. A significant reduction in fluorescence intensity was recorded (Fig. 3) as the concentration of CO was increased from 9.7×10^{-5} M to 2.6×10^{-5} M, thereby indicating the successful quenching of N-CQDs. Additionally, results from UV-visible titration corroborated the observation of a consistent decline in N-CQD fluorescence with increasing CO concentration (Fig. S4†). These findings confirm the capacity of N-CQDs to detect CO *via* fluctuations in both fluorescence and UV intensity. Subsequent regression analysis was conducted to ascertain the binding affinity of N-CQDs for CO, which yielded a value of 3.055×10^4 M^{-1} (Fig. S5†). An exceptional linear correlation between fluorescence intensity and CO concentration was identified within the range of 2.43–47.51 μM, exhibiting a correlation coefficient (R^2) of 0.99836 (Fig. S6†). The limits of

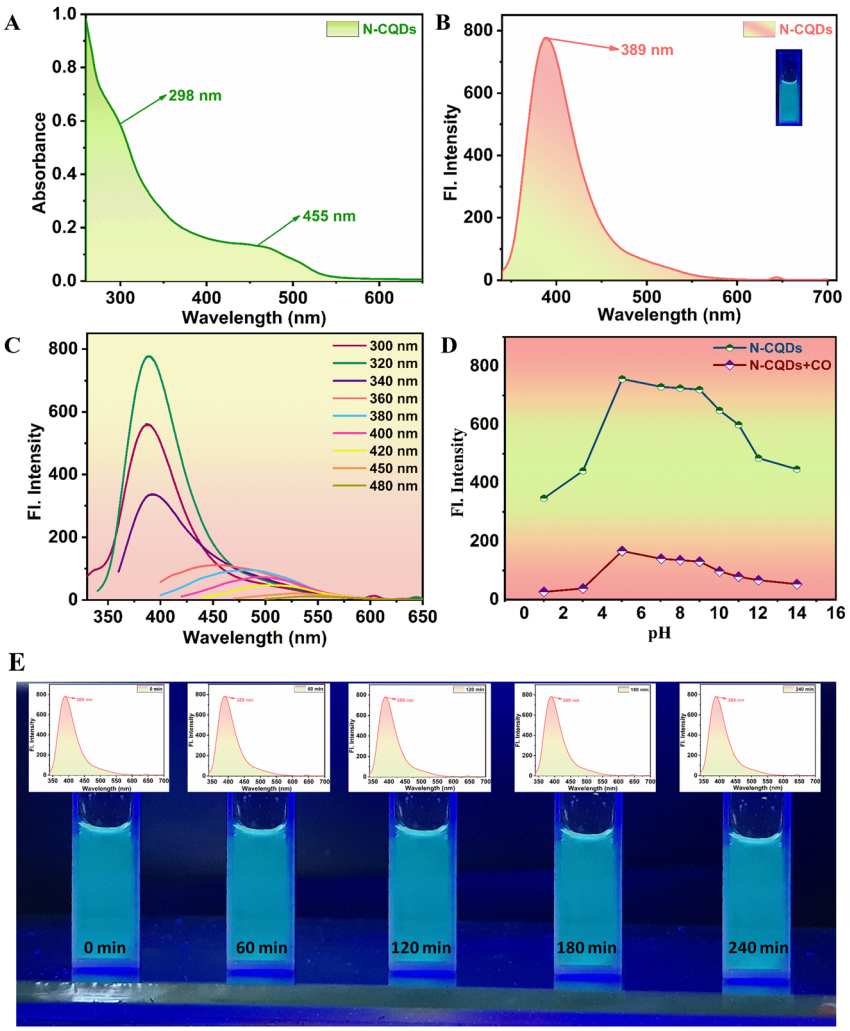

Fig. 2 Spectrophotometric analyses of N-CQDs: (A) UV-vis absorption spectrum. (B) Fluorescence emission spectrum. (C) Emission spectra under different excitation wavelengths. (D) pH response measurement of N-CQDs and N-CQDs + CO. (E) Photostability test of N-CQDs under continuous irradiation with 365 nm UV light.

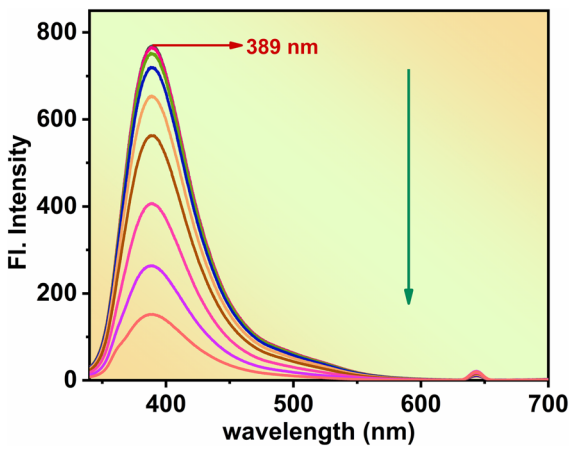

Fig. 3 Fluorescence emission spectra of N-CQDs upon addition of CO (10^{-4} M).

detection (LOD) and quantification (LOQ) for CO were determined to be 0.102 μM and 0.341 μM utilizing the formulas $3\sigma/m$ and $10\sigma/m$, respectively, where m denotes the slope of the calibration curve and σ represents the standard deviation (Table S2†). Comprehensive selectivity tests (Fig. S7†) demonstrated that the fluorescence of N-CQDs experienced substantial quenching in the presence of CO, while other analytes tested exhibited negligible effects, thereby underscoring the high selectivity of N-CQDs for CO detection. The integration of fluorescence spectroscopy alongside UV-visible absorption analyses provides foundational insights into the interaction mechanisms at play, while FT-IR, DLS, and XPS analyses furnish more detailed information regarding the specific chemical interactions and functional groups involved. The selective affinity of these N-CQDs for CO is attributed to the meticulous arrangement of surface functional groups, enhanced interaction sites resulting from nitrogen doping, and the complementary dimensions and morphology. Moreover, their distinctive fluorescence response, compatibility with environ-

mental conditions, and capacity for aggregation with CO contribute to the simultaneous quenching of fluorescence, thus reinforcing their strong selective affinity toward CO.

Probable quenching mechanism discussion

A comprehensive series of studies was undertaken to understand how CO induces the quenching of N-CQDs. Fluorescence quenching may occur *via* multiple mechanisms, including static quenching, dynamic quenching, or a combination of these pathways. To elucidate the specific quenching mechanism of N-CQDs by CO, the Stern–Volmer equation[28,34] was applied (eqn (2)) as a methodological framework. This involved plotting the ratio F_0/F against the concentration of the quencher, [Q], where F_0 and F represent the fluorescence intensities of N-CQDs in the absence and presence of CO (the quencher), respectively, while K is the Stern–Volmer quenching constant. A linear relationship was anticipated in scenarios characterized by either static or dynamic quenching, a result that was corroborated by the experimental findings obtained in this study (Fig. 4A).

$$F_0/F = 1 + K[\mathrm{Q}] \quad (2)$$

For scenarios involving both dynamic and static quenching, the Stern–Volmer plot can be expressed as follows.

$$F_0/F = (1 + K_\mathrm{D}[\mathrm{Q}])(1 + K_\mathrm{S}[\mathrm{Q}]) \quad (3)$$

Analysis suggests that a plot of F_0/F against [Q] should exhibit an upward curve. Nevertheless, such a curvature was not observed in the results obtained (see Fig. 4A). Therefore, the hypothesis regarding the existence of combined mechanisms was rejected.

Fluorescence lifetime measurements were performed to elucidate the quenching mechanism associated with N-CQDs. The average fluorescence lifetimes of the N-CQDs were determined to be 1.51 ns in the absence of CO and 1.71 ns when CO was present, as detailed in Table S3.† As depicted in Fig. 4C and presented in Table S3,† the addition of CO did not elicit a significant alteration in fluorescence lifetime values, suggesting that N-CQDs engage with CO in the ground state through a process of static quenching, thereby negating the possibility of dynamic quenching.[35]

Additionally, UV-vis spectroscopy assessments were performed to further validate static quenching resulting from complex formation in the ground state. The findings illustrated in Fig. S4† indicate a shift in the absorption peak of N-CQDs following the addition of CO, which supports the conclusion of ground state complex formation and confirms the occurrence of static quenching. A modified Stern–Volmer equation was employed to substantiate the existence of the ground-state complex through the mechanism of static quenching.

$$K_\mathrm{app} = (F_0/F - 1)/[\mathrm{Q}] = (K_\mathrm{S} + K_\mathrm{D}) + K_\mathrm{S}K_\mathrm{D}[\mathrm{Q}] \quad (4)$$

By graphing $(F_0/F - 1)/[\mathrm{Q}]$ *vs.* [Q], a linear correlation was anticipated, thereby suggesting that the quenching process is likely facilitated by the formation of such a ground-state complex, as evidenced in this study (Fig. 4B).[36]

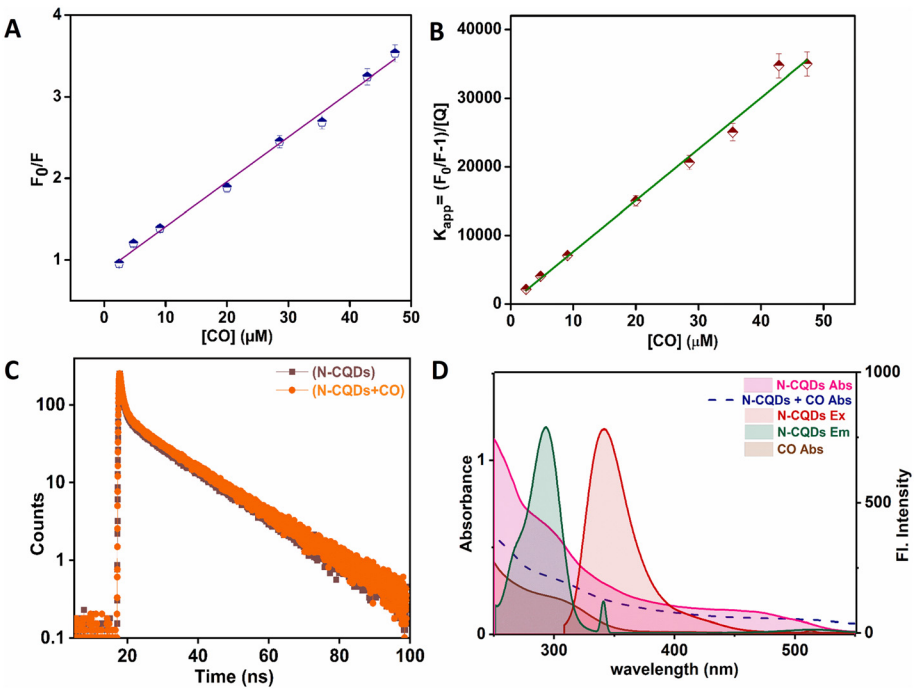

Fig. 4 (A) Second-order polynomial fitting of the Stern–Volmer plot for CO. (B) Plot of K_app *vs.* concentration of CO. (C) Fluorescence lifetime of N-CQDs before (Brown) and after the addition of CO (Orange). (D) Excitation spectra (Red gradient) and emission spectra (Green line) of N-CQDs, absorption spectra of N-CQDs (Pink line), CO (Brown line) and N-CQDs + CO (Navy Blue gradient).

On the other hand, the overlap observed between the fluorescence emission and/or excitation spectra of the fluorophore, specifically N-CQDs, and the absorption band of the quencher, CO, indicates the occurrence of an inner filter effect (IFE), which was also substantiated by the results of this study (Fig. 4D).[37]

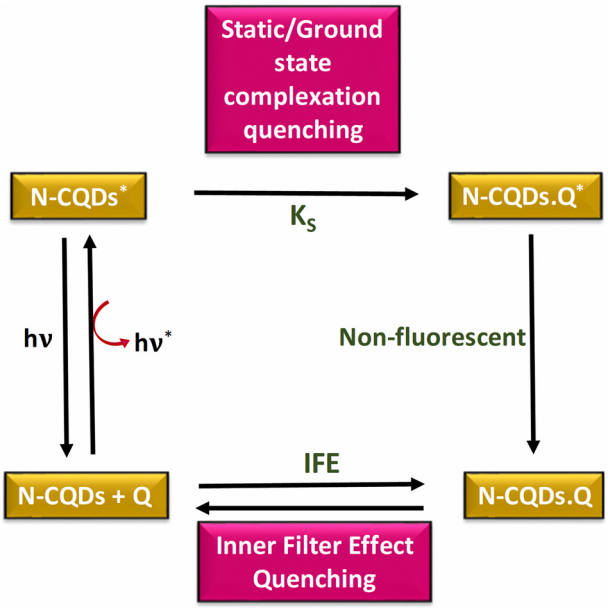

Fig. 5 Schematic of the combined static quenching and inner filter effect (IFE) of N-CQDs by the quencher (Q) CO.

In conclusion, it can be asserted that the quenching mechanism of N-CQDs is primarily attributed to static quenching, which occurs through the formation of ground-state complexes, as well as the IFE (Fig. 5).

Seed germination in the presence of CO

An experimental investigation was conducted to study seed germination under varying conditions involving carbon monoxide (CO). The study utilized black chickpeas and mung beans, which were categorized into three distinct sets: the first set was soaked in water (Fig. 6A), the second in a solution comprising ruthenium/cadmium metal (Fig. 6B), and the third in a solution containing a carbon monoxide-releasing compound (tricarbonylchloro(glycinato) ruthenium(II), CORM) (Fig. 6C). Normal seed germination was observed in both the water-soaked and CORM-treated sets, whereas no germination occurred in the ruthenium/cadmium metal solution, a phenomenon likely attributable to the stress induced by heavy metals. Despite the presence of ruthenium/cadmium in set three, seed germination proceeded, attributed to CO release from the CORM compound. These observations indicate the significant role of CO in mitigating heavy metal-induced stress, enabling successful seed germination in challenging environments. Furthermore, the presence of CO within plant systems was effectively monitored employing N-CQDs and confocal microscopy. The findings designate the synthesized N-CQDs to serve as a reliable tool for detecting CO within biological systems, particularly in circumstances where CO reduces heavy metal stress.

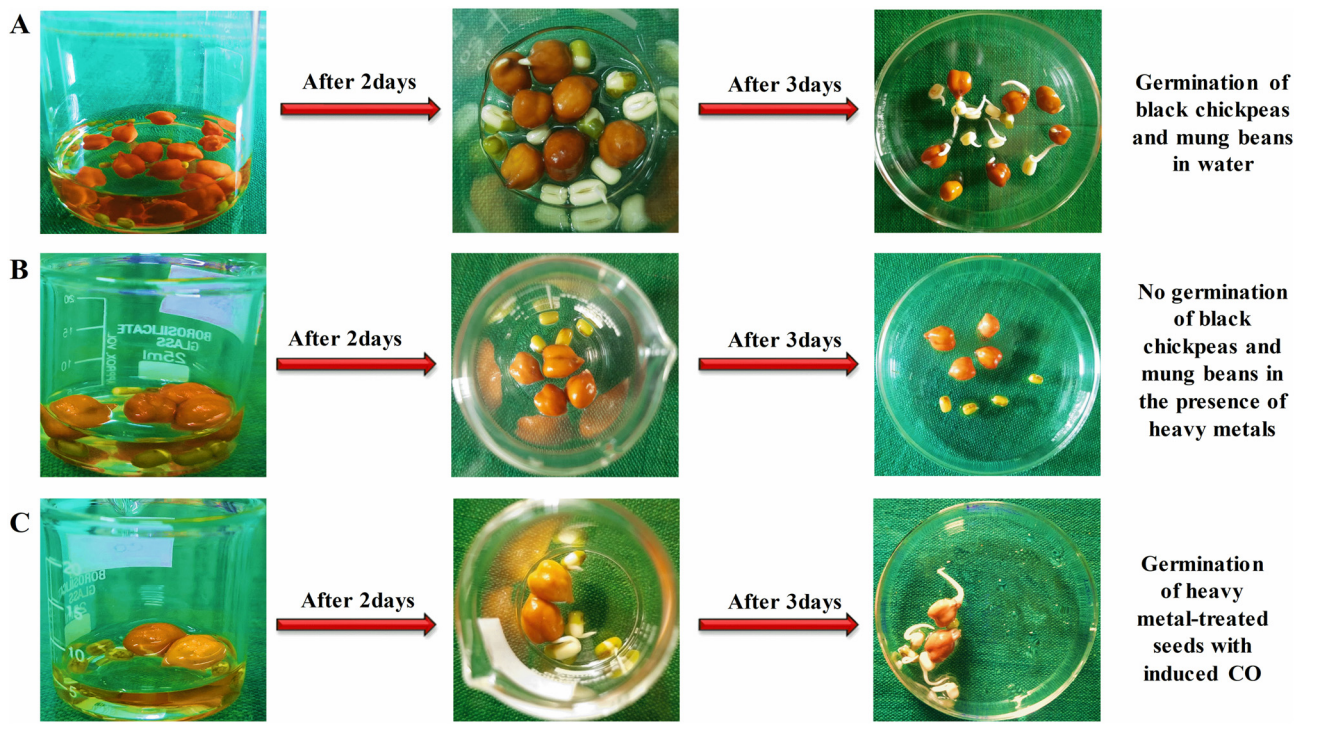

Fig. 6 Schematic representation of the effect of CO on seed germination under heavy metal stress (A–C).

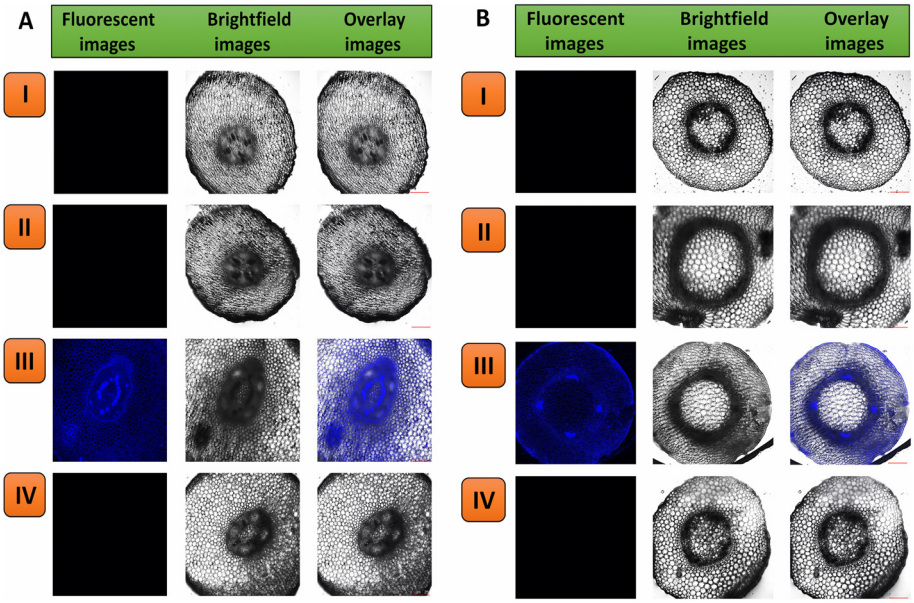

Fig. 7 Confocal microscopy images of transverse sections of the root of (A) black chickpeas (*Cicer arietinum*) and (B) mung bean (*Vigna radiata*) after treatment with quantum dots (N-CQDs), carbon monoxide (CO), and heavy metals. (AI–BI) Control root section; (AII–BII) root section exposed to 10^{-3} M of heavy metal; (AIII–BIII) root section exposed to 10^{-3} M of N-CQDs following prior exposure to heavy metals; (AIV–BIV) root section pre-treated with CO (10^{-3} M) after treatment with heavy metal and N-CQDs. The left, middle, and right panels display fluorescent images, brightfield images, and overlay images, respectively. Magnification: 100×. Zoom factor: 0.75. Scale bars: 0–250 μm.

Biological quantitative analysis by confocal laser scanning microscopy

Using confocal laser scanning microscopy, it was observed that the N-CQDs effectually entered live plant cells and interacted with analytes, *i.e.*, CO and heavy metals. The N-CQDs fluorescent signal was used to observe endocytosis, allowing for the study and investigation of cellular uptake processes. Fig. 7 distinctly establishes diffusion of the probe into live cells of embryonic roots and seeds of black chickpeas and mung beans, as shown by the vivid blue fluorescence. This corroborates the ability of N-CQDs to traverse cellular membranes in both plant species.

No fluorescence was detected in the transverse slices of the embryonic roots and seeds of the untreated (Con) (Fig. 7AI–BI and S8AI–BI†) and heavy metal-treated (Fig. 7AII–BII and S8AII–BII†) black chickpea and mung bean plants. The sections of the embryonic roots and seeds of both the plants treated with heavy metal and N-CQDs (Fig. 7AIII–BIII and S8AIII–BIII†) exhibited intense blue fluorescent signals. The transverse sections of the black chickpea and mung bean plant embryonic roots and seeds exposed to both the analyte CO and the probe N-CQDs (Fig. 7AIV–BIV and S8AIV–BIV†) exhibited no fluorescence, plainly signifying that the analyte quenches the fluorescent properties of the probe.

In the embryonic root sections of both plants, the blue fluorescence signal was detected in the epidermis (outermost layer) and the endodermis (innermost layer). However, the intensity of the blue fluorescence was higher in the endodermal layer than in the epidermal layer. This suggests that the accumulation of N-CQDs was more in the endodermal region of the embryonic root of the two plants. The internalization of N-CQDs into the dicotyledonous seeds of black chickpea and mung bean was verified *via* blue fluorescence as the N-CQDs accumulated in the procambium within the embryo of the seeds, which is a precursor tissue that will ultimately mature into xylem and phloem during germination.

Discussion

Confocal microscopy confirmed that the N-CQDs successfully penetrated the intracellular spaces and interacted with the analytes, as observed in transverse sections of black chickpea and mung bean embryonic roots and seeds. The embryonic roots and seed sections treated with the combination of heavy metals and N-CQDs exhibited a blue fluorescent signal. The fluorescence was brighter in different regions of the embryonic roots and seeds of the plants due to the varied assimilation of the probe. Nevertheless, these sections treated with CO and N-CQDs did not exhibit any fluorescence, indicating that CO suppresses the fluorescence of N-CQDs.

Confocal microscopy enabled the detailed analysis of black chickpea and mung bean embryonic roots and seeds cross-sections, confirming the penetration of probe and analytes and interaction within intracellular spaces. This showed insights into fluorescence differences and the mechanisms behind intracellular substance interactions. Densitometric analysis (Fig. S9†) of the fluorescence signal validates a sufficient amount of blue luminance of N-CQDs in roots and seeds.

Thus, it can be concluded that the produced N-CQDs function as a viable sensing tool for monitoring the presence or absence of CO in plants that could be utilized in the investigations of participation in several physiological activities in signaling and healing processes.

Conclusions

This study elucidates the dual characteristics of carbon monoxide (CO) as a hazardous gas to humans, which also functions as a crucial signaling molecule within plant systems, facilitating germination and enabling adaptation to adverse environmental conditions. Monitoring the presence of CO and its functions in plants carries substantial implications for advancing comprehension of its biological activities. To address this imperative, nitrogen-doped carbon quantum dots (N-CQDs) were developed, characterized by low toxicity, ease of synthesis, cost-effectiveness, exemplary biocompatibility, and minimal environmental impact. These nanodots demonstrate the ability to selectively detect CO through a quenching mechanism, presenting an innovative method for tracking CO within plant systems. In spectroscopic investigations, the nanodots used for monitoring CO binding were successfully executed, with confirmation achieved through confocal microscopy, which provided visual evidence of CO interactions at the cellular level in the plant system. Consequently, N-CQDs are identified as an effective and reliable nanomarker for tracking CO in plant systems, suggesting significant potential applications in studying plant stress responses, germination, and developmental processes. This study indicates the broad applicability and assurance of the sensor in enhancing plant research, particularly in the context of germination and environmental stress conditions.

Author contributions

SM: done with formal analysis, investigation, data collection, experiment, visualization, validation, methodology, original draft writing, and editing, OS: procured confocal imaging and helped in writing the biological part. SMM: helped to record XPS data. AC: contributed to all of the biological experiments. PS: brought forward the concept, designing experiments, data curation, script reviewing and editing, visualized and supervised the investigation, and funding acquisition.

Data availability

The data supporting this article have been included as part of the ESI.†

Conflicts of interest

There are no conflicts to declare.

Acknowledgements

P.S. acknowledges SERB, India, for awarding her SERB power grant [Project file no. Ref. No. SPG/2020/000713]. The authors sincerely acknowledge the Department of Chemistry, Visva-Bharati, Santiniketan, West Bengal, India. The authors also acknowledge Shubhankar Ghorai, IIEST, Shibpur, for helping with the data collection of TCSPC and Sourav Chakraborty, Department of Biotechnology, IIT Kharagpur with the data collection of XPS. The authors thank the Department of ISERC, Visva-Bharati University, India for the assistance with FT-IR, funded by DST FIST (Ref. No. SR/FST/CS-I/2017/21).

References

1 Y. J. Xie, T. Ling, Y. Han, K. Liu, Q. Zheng, L. Huang, X. Yuan, Z. He, B. Hu, L. Fang, Z. Shen, Q. Yang and W. Shen, *Plant, Cell Environ.*, 2008, **31**, 1864–1881.
2 K. Liu, S. Xu, W. Xuan, T. Ling, Z. Cao, B. Huang, Y. Sun, L. Fang, Z. Liu, N. Zhao and W. Shen, *Plant Sci.*, 2007, **172**, 544–555.
3 Y. H. Liu, S. Xu, T. F. Ling, L. L. Xu and W. B. Shen, *J. Plant Physiol.*, 2010, **167**, 1371–1379.
4 T. F. Ling, B. Zhang, W. T. Cui, M. Z. Wu, J. S. Lin and W. T. Zhou, *Plant Sci.*, 2009, **177**, 331–340.
5 D. K. Meng, J. Chen and Z. M. Yang, *J. Hazard. Mater.*, 2011, **186**, 1823–1829.
6 M. Bilban, A. Haschemi, B. Wegiel, B. Y. Chin, O. Wagner and L. E. Otterbein, *J. Mol. Med.*, 2008, **86**, 267–279.
7 H. Bahrmann and B. Cornils, New Syntheses with Carbon Monoxide, Springer-Verlag, Berlin, Germany, 1980.
8 W. Xuan, F. Y. Zhu, S. Xu, B. K. Huang, T. F. Ling, J. Y. Qi, M. B. Ye and W. B. Shen, *Plant Physiol.*, 2008, **148**, 881–893.
9 L. Feng, L. Wei, Y. Liu, J. Ren and W. Liao, *Nitric Oxide*, 2023, **138–139**, 51–63.
10 M. Wang and W. Liao, *Front. Plant Sci.*, 2016, **7**, 572.
11 D. M. Santa-Cruz, N. A. Pacienza, A. H. Polizio, K. B. Balestrasse, M. L. Tomaro and G. G. Yannarelli, *Phytochemistry*, 2010, **71**, 1700–1707.
12 Y. T. Lin, W. Zhang, F. Qi, W. T. Cui, Y. J. Xie and W. B. Shen, *J. Plant Physiol.*, 2014, **171**, 1–8.
13 J. Dekker and M. Hargrove, *Am. J. Bot.*, 2002, **89**, 410–416.
14 W. Cui, F. Qi, Y. Zhang, H. Cao, J. Zhang, R. Wang and W. Shen, *Plant Cell Rep.*, 2015, **34**, 435–445.
15 Y. Xie, C. Zhang, D. Lai, Y. Sun, M. K. Samma, J. Zhang and W. Shen, *J. Plant Physiol.*, 2014, **171**(2), 53–62.
16 R. Atchudan, S. C. Kishore, P. Gangadaran, T. N. J. I. Edison, S. Perumal, R. L. Rajendran, M. Alagan, S. Al-Rashed, B. C. Ahn and Y. R. Lee, *Environ. Res.*, 2022, **204**, 112365.
17 R. Atchudan, T. N. J. I. Edison, S. Perumal, N. Muthuchamy and Y. R. Lee, *Fuel*, 2020, **275**, 117821.

18 R. Atchudan, T. N. J. I. Edison, S. Mani, S. Perumal, R. Vinodh, S. Thirunavukkarasu and Y. R. Lee, *Dalton Trans.*, 2020, **49**, 17725–17736.
19 R. Atchudan, T. N. J. I. Edison, S. Perumal, R. Vinodh and Y. R. Lee, *J. Mol. Liq.*, 2019, **296**, 111817.
20 R. Atchudan, T. N. J. I. Edison, K. R. Aseer, S. Perumal, N. Karthik and Y. R. Lee, *Biosens. Bioelectron.*, 2018, **99**, 303–311.
21 Md. P. Sk and A. Chattopadhyay, *RSC Adv.*, 2014, **4**, 31994–31999.
22 W. Peng, L. Wei, W. Qiong, L. Yushan and L. Shouxin, *RSC Adv.*, 2017, **7**, 44144–44153.
23 Y. Zheng, D. Yang, X. Wu, H. Yan, Y. Zhao, B. Feng, K. Duan, J. Weng and J. Wang, *RSC Adv.*, 2015, **5**, 90245–90254.
24 J. Shen, S. Shang, X. Chen, D. Wang and Y. Cai, *Sens. Actuators, B*, 2017, **248**, 92–100.
25 S. Cai, Q. Houjuan, M. Rongxiu, S. Zhe, X. Lidong, W. Guangbiao, H. Zhanhua, L. Shouxin, L. Jian, D. Mengyao, F. Jincheng and G. Zhanhu, *Mater. Sci. Eng., C*, 2019, **105**, 110132.
26 F. Jie, Z. Xiaoran, B. Wei and T. Xinjing, *Mater. Chem. Front.*, 2019, **3**, 2751–2758.
27 L. Wenjing, J. Yuan, G. Yifang, Q. Jie, M. Maedeh, S. Shaomin, D. Chuan and Z. Chen, *ACS Appl. Mater. Interfaces*, 2018, **10**(49), 42915–42924.
28 S. Mondal, O. Sarkar, J. Raut, S. M. Mandal, A. Chattopadhyay and P. Sahoo, *ACS Appl. Bio Mater.*, 2024, **7**(7), 4690–4701.
29 Y. M. AlZahrani, S. Alharthi, H. A. AlGhamdi, A. O. Youssef, S. S. Ahmed, E. H. Mohamed, S. A. Mahmoud and M. S. Attia, *RSC Adv.*, 2023, **13**, 21318.
30 C. Shi, H. Qi, R. Ma, Z. Sun, L. Xiao, G. Wei, Z. Huang, S. Liu, J. Li, M. Dong, J. Fan and Z. Guo, *Mater. Sci. Eng., C*, 2019, **105**, 110132.
31 Y. Wang, S. H. Kim and L. Feng, *Anal. Chim. Acta*, 2015, **890**, 134–142.
32 H. Li, X. He, Y. Liu, H. Huang, S. Lian, S.-T. Lee and Z. Kang, *Carbon*, 2011, **49**(2), 605–609.
33 H. Wang, P. Sun, S. Cong, J. Wu, L. Gao, Y. Wang, X. Dai, Q. Yi and G. Zou, *Nanoscale Res. Lett.*, 2016, **11**(1), 27.
34 J. Raut, R. D. Sherpa, S. K. Jana, S. M. Mandal, S. Mandal, S. P. Hui and P. Sahoo, *ACS Appl. Nano Mater.*, 2023, **6**, 23611–23619.
35 R. L. Joseph, in *Principles of Fluorescence Spectroscopy*, Kluwer Academic/Plenum Publishers, New York, 2nd edn, 1999.
36 S. Mondal, J. Raut, O. Sarkar, S. M. Mandal, A. Chattopadhyay and P. Sahoo, *New J. Chem.*, 2023, **47**, 20859–20865.
37 S. A. Tanwar, R. Parui, R. Garai, A. M. Chanu and K. P. Iyer, *ACS Meas. Sci. Au*, 2022, **2**, 23–30.